The Nonlinear Tensor Diffusion in Segmentation of Meaningful Biological Structures from Image Sequences of Zebrafish Embryogenesis

Olga Drblíková[1], Karol Mikula[1], and Nadine Peyriéras[2]

[1] Slovak University of Technology, Radlinského 11, 813 68 Bratislava, Slovakia
olga.drblikova@stuba.sk, karol.mikula@stuba.sk
http://www.math.sk/drblikov, http://www.math.sk/mikula
[2] CNRS-DEPSN, Institut de Neurobiologie Alfred Fessard, Batiment 32-33, Avenue de la Terrasse, 91198 Gif sur Yvette, France
nadine.peyrieras@iaf.cnrs-gif.fr

Abstract. In this contribution we develop a strategy for segmentation of evolving biological structures in image sequences. Our approach is based on combination of nonlinear tensor diffusion image smoothing and subjective surface based image segmentation. Since the fine cell structure would restrain the evolving segmentation function to achieve a shape of meaningful biological structures, we have to smooth properly the images in the sequence. To that goal we apply the nonlinear tensor diffusion which enhances the connectivity of bordering structure lines and smoothes their inner parts. For the numerical implementations we use semi-implicit diamond-cell finite volume methods both for filtering and segmentation. We show application of the method in image segmentation of early stages of zebrafish embryogenesis.

1 Introduction

The subjective surface based segmentation is an efficient tool for the extraction of 2D or 3D image objects, cf. [10,9,1]. It is also the case when dealing with two-photon laser scanning microscopy images in detecting and segmenting structures at cellular and subcellular level, cf. [6, 8]. However, the use of such algorithms when segmenting the supercellular structures is not straightforward. Using an original (not filtered) image leads to entirely useless results due to the presence of small cell structures. Then a useful tool is filtering by the nonlinear tensor diffusion enhancing the coherence of structure boundaries and smoothing the inner cell structures and noise. The model, cf. [11, 7, 4], has the following form

$$\partial_t u - \nabla \cdot (D\nabla u) = 0, \qquad \text{in } Q_T \equiv I \times \Omega, \tag{1}$$

$$u(x,0) = u_0(x), \quad \text{in } \Omega, \tag{2}$$

$$(D\nabla u) \cdot \mathbf{n} = 0, \qquad \text{on } I \times \partial\Omega, \tag{3}$$

where u represents a greylevel 3D image intensity, $u_0 \in L^2(\Omega)$, $I = [0, T]$ denotes a time interval, Ω is an image domain, $D = D(u(x,t))$ is a diffusion tensor and

X.-C. Tai et al. (Eds.): SSVM 2009, LNCS 5567, pp. 63–74, 2009.

n is the outer normal unit vector to $\partial\Omega$. The model is useful when a strong filtering is desirable in a preferred direction, e.g. along 2D edge surfaces in 3D images and a low smoothing is expected in the perpendicular direction.

2 Design of the Diffusion Tensor

The matrix D depends on a smoothed intensity gradient, which is given as

$$\nabla u_{\tilde{t}} = (u_{x_1}, u_{x_2}, u_{x_3})^T, \text{ where } \quad u_{\tilde{t}}(x,t) = (G_{\tilde{t}} * u(\cdot,t))(x), \quad (\tilde{t} > 0) \tag{4}$$

and $G_{\tilde{t}}$ is a Gaussian kernel. Provided $\mu = ||\nabla u_{\tilde{t}}||^2 > 0$ we choose a triplet of vectors (v_1, v_2, v_3) as follows

$$v_1 \parallel \nabla u_{\tilde{t}}, \qquad v_2 \perp \nabla u_{\tilde{t}}, \qquad v_3 \perp \nabla u_{\tilde{t}}, \qquad v_2 \perp v_3\,. \tag{5}$$

The direction of vector v_1 corresponds to the direction of the largest intensity change. The other two vectors give a tangential plane to a level set of image intensity which may represent a 2D surface edge in a 3D image, provided that μ is large. It is called a coherence plane $\mathcal{P}$, cf. [4, 7], and corresponds to an eigenspace corresponding to the eigenvalue 0 of the outer product $\nabla u_{\tilde{t}} \otimes \nabla u_{\tilde{t}}$. In order to improve the coherence, the diffusion tensor D must steer a filtering process such that the diffusion is strong and increasing with the level of μ along the coherence plane and is small in the perpendicular direction. We achieve it choosing the eigenvalues of the diffusion tensor, which determine the diffusivities in the directions v_1, v_2 and v_3 as

$$\begin{aligned} &\kappa_1 = \alpha, \quad \alpha \in (0,1),\ \alpha \ll 1, \\ &\kappa_2 = \begin{cases} \alpha, & \text{if } \mu = 0, \\ \alpha + (1-\alpha)\exp\left(\frac{-C}{\mu}\right), & C > 0 \quad \text{otherwise.} \end{cases} \end{aligned} \tag{6}$$

Further, we apply other convolution with a smoothing kernel ρ to get the diffusion matrix D in the form

$$D = G_\rho * D_0, \text{ where } D_0 = \begin{cases} B, & \text{if } \mu = 0, \\ PBP^{-1} & \text{otherwise,} \end{cases} \quad B = \begin{pmatrix} \kappa_1 & 0 & 0 \\ 0 & \kappa_2 & 0 \\ 0 & 0 & \kappa_2 \end{pmatrix} \tag{7}$$

and P represents a transition matrix from the basis (v_1, v_2, v_3) to (e_1, e_2, e_3). The exponential function in (6) is used to ensure that κ_2 does not exceed 1. The process never stops owing to the positive parameter α. Even if μ tends to zero, a small linear diffusion with a diffusivity $\alpha > 0$ still remains there. C has the role of a threshold parameter. If $\mu \gg C$ then $\kappa_2 \approx 1$, and, conversely if $\mu \ll C$ then $\kappa_2 \approx \alpha$.

After some manipulations we get that at any point where $\mu > 0$, the matrix D_0 has the following form

$$\frac{1}{\mu}\begin{pmatrix} u_{x_1}^2\kappa_1 + (u_{x_2}^2 + u_{x_3}^2)\kappa_2 & u_{x_1}u_{x_2}(\kappa_1 - \kappa_2) & u_{x_1}u_{x_3}(\kappa_1 - \kappa_2) \\ u_{x_1}u_{x_2}(\kappa_1 - \kappa_2) & u_{x_2}^2\kappa_1 + (u_{x_1}^2 + u_{x_3}^2)\kappa_2 & u_{x_2}u_{x_3}(\kappa_1 - \kappa_2) \\ u_{x_1}u_{x_3}(\kappa_1 - \kappa_2) & u_{x_2}u_{x_3}(\kappa_1 - \kappa_2) & u_{x_3}^2\kappa_1 + (u_{x_1}^2 + u_{x_2}^2)\kappa_2 \end{pmatrix} \tag{8}$$

in the standard basis (e_1, e_2, e_3). Such choice of the matrix D_0 was given in [4], it is independ on a concrete choice of v_2 and v_3 and can be directly and fast evaluated using the diamond-cell finite volume technique (see also next section). Then the matrices are spatially averaged using the Gaussian smoothing with a variance ρ to get the final matrix D elements. The diffusion tensor possesses the smoothness, symmetry and positive definiteness properties, cf. [4].

3 The Finite Volume Scheme for 3D Nonlinear Tensor Diffusion

Let the image $u(x)$ be represented by a bounded mapping $u : \Omega \to R$ and given by $n_1 \times n_2 \times n_3$ voxels (finite volumes) such that it looks like a mesh with n_1 rows, n_2 columns and n_3 layers. Let us consider an image domain $\Omega = (0, n_1 h) \times (0, n_2 h) \times (0, n_3 h)$, with a voxel size h. We consider the diffusion process in a time interval $I = [0, T]$. Let the time discretization is given by $0 = t_0 < t_1 < ... < t_{N_{max}} = T$ with $t_n = t_{n-1} + k$, where k is a length of a discrete time step. We will look for an approximation of solution at time t_n for every $n = 1, ..., N_{max}$.

We start the scheme derivation integrating the equation (1) over a finite volume K, then provide a semi-implicit time discretization and use the divergence theorem to have

$$\frac{u_K^n - u_K^{n-1}}{k} m(K) - \sum_{\sigma \in \mathcal{E}_K \cap \mathcal{E}_{int}} \int_\sigma (D^{n-1} \nabla u^n) \cdot \mathbf{n}_{K,\sigma} ds = 0, \tag{9}$$

where u_K^n, $K \in \mathcal{T}_h$, denotes the mean value of u^n on K and $\mathcal{T}_h$ is a cubic finite volume mesh. Further quantities and notations are given as follows: $m(K)$ is the 3D measure of finite volume K with the boundary ∂K, $\sigma_{KL} = K \cap L$ is a side of the finite volume K, where $L \in \mathcal{T}_h$ is a neighboring finite volume to K for which holds that the volumes K and L share a 2D surface element with a nonzero area. At several places we will replace σ_{KL} by σ only due to a notation simplification. $\mathcal{E}_K$ represents the set of sides such that $\partial K = \bigcup_{\sigma \in \mathcal{E}_K} \sigma$ and $\mathcal{E} = \bigcup_{K \in \mathcal{T}_h} \mathcal{E}_K$. The set of boundary sides is denoted by $\mathcal{E}_{ext}$, that is $\mathcal{E}_{ext} = \{\sigma \in \mathcal{E}, \sigma \subset \partial\Omega\}$ and $\mathcal{E}_{int} = \mathcal{E} \setminus \mathcal{E}_{ext}$. Υ is the set of pairs of neighboring finite volumes defined by $\Upsilon = \{(K, L) \in \mathcal{T}_h^2,\ K \neq L,\ m(K \cap L) \neq 0\}$ and $\mathbf{n}_{K,\sigma}$ is the normal unit vector to σ outward to K.

Our discrete approximation solution is defined as

$$u_{h,k}(x, t) = \sum_{n=0}^{N_{max}} \sum_{K \in \mathcal{T}_h} u_K^n \chi\{x \in K\} \chi\{t_{n-1} < t \leq t_n\}, \tag{10}$$

where the function $\chi(A)$ is given by

$$\chi_{\{A\}} = \begin{cases} 1, & \text{if } A \text{ is true,} \\ 0, & \text{elsewhere.} \end{cases}$$

The finite volume approximation at the n-th time step is given by $u^n_{h,k}(x) = \sum_{K\in\mathcal{T}_h} u^n_K \chi\{x \in K\}$ and initial values as $u^0_K = \frac{1}{m(K)} \int_K u_0(x)dx$, $K \in \mathcal{T}_h$. We can define an auxiliary unknown $\phi^n_\sigma(u^n_{h,k})$ representing an approximation of the exact averaged flux $\frac{1}{m(\sigma)} \int_\sigma (D^{n-1}\nabla u^n) \cdot \mathbf{n}_{K,\sigma} ds$ for any K and $\sigma \in \mathcal{E}_K$ in order to rewrite (9) in the form

$$\frac{u^n_K - u^{n-1}_K}{k} - \frac{1}{m(K)} \sum_{\sigma\in\mathcal{E}_K\cap\mathcal{E}_{int}} \phi^n_\sigma(u^n_{h,k}) m(\sigma) = 0,$$

where $m(\sigma)$ is the measure of side σ.

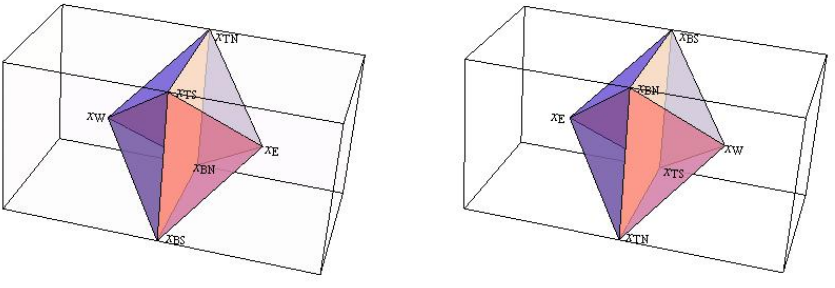

Fig. 1. The co-volumes associated with the side $\sigma = \sigma_{WE}$ (left) and $\sigma = \sigma_{EW}$ (right)

$\phi^n_\sigma(u^n_{h,k})$ is built with the help of a co-volume mesh, cf. e.g. [2, 3], for the 2D case. We create a co-volume χ_σ associated with σ around each finite volume side by joining four vertices of this side and midpoints of the finite volumes which are common to this side, cf. Fig. 1. The co-volume boundary consists of triangles $\bar{\sigma} \subset \partial\chi_\sigma$ (their vertices are denoted by $N_1(\bar{\sigma})$, $N_2(\bar{\sigma})$ and $N_3(\bar{\sigma})$) and $\mathbf{n}_{\chi_\sigma,\bar{\sigma}}$ is the normal unit vector to $\bar{\sigma}$ outward to χ_σ. First, we approximate the averaged gradient on χ_σ. Applying the divergence theorem we obtain $\frac{1}{m(\chi_\sigma)} \int_{\chi_\sigma} \nabla u^n dx = \frac{1}{m(\chi_\sigma)} \int_{\partial\chi_\sigma} u^n \mathbf{n}_{\chi_\sigma,\bar{\sigma}} ds$ which can be approximated as follows $p^n_\sigma(u) = \frac{1}{m(\chi_\sigma)} \sum_{\bar{\sigma}\in\partial\chi_\sigma} \frac{1}{3} \left(u^n_{N_1(\bar{\sigma})} + u^n_{N_2(\bar{\sigma})} + u^n_{N_3(\bar{\sigma})} \right) m(\bar{\sigma}) \mathbf{n}_{\chi_\sigma,\bar{\sigma}}$. The values at x_E and x_W are denoted as u_E and u_W. Further, we evaluate the values u_{TN}, u_{TS}, u_{BN}, and u_{BS} at the vertices x_{TN}, x_{TS}, x_{BN}, and x_{BS}, cf. Fig. 1, as the arithmetic mean of u_K, where K represents the finite volumes which are common to the vertex. Since the mesh is uniform and squared, we can simplify our discrete scheme applying the following relations: $m(\chi_\sigma) = \frac{h^3}{3}$, $m(\bar{\sigma}) = \frac{\sqrt{2}}{4} h^2$. After a short calculation we can state

$$p^n_\sigma(u) = \frac{u^n_E - u^n_W}{h} \mathbf{n}_{K,\sigma} + \frac{u^n_{TN} + u^n_{BN} - u^n_{TS} - u^n_{BS}}{2h} \mathbf{t1}_{K,\sigma} + \frac{u^n_{TN} + u^n_{TS} - u^n_{BN} - u^n_{BS}}{2h} \mathbf{t2}_{K,\sigma}, \tag{11}$$

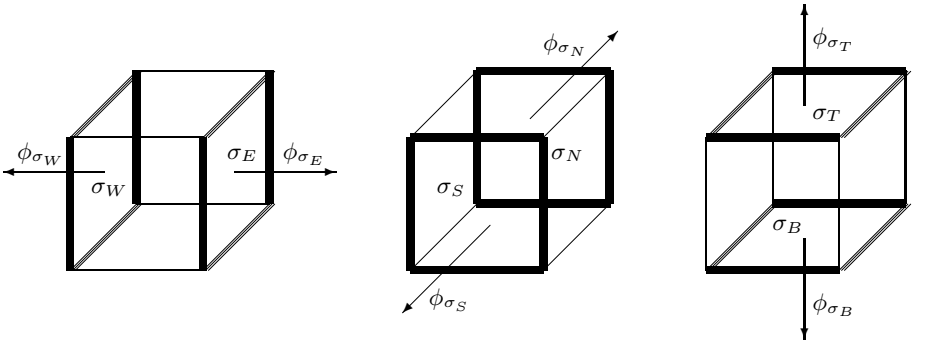

Fig. 2. A finite volume K, its boundaries σ_i, $i = E, W, N, S, T, B$ and the fluxes outward to the finite volume K

where $\mathbf{t1}_{K,\sigma}$ is a unit vector parallel to $x_{TN} - x_{TS}$ such that $(x_{TN} - x_{TS}) \cdot \mathbf{t1}_{K,\sigma} > 0$ and $\mathbf{t2}_{K,\sigma}$ is a unit vector parallel to $x_{TN} - x_{BN}$ such that $(x_{TN} - x_{BN}) \cdot \mathbf{t2}_{K,\sigma} > 0$.

We replace the exact gradient ∇u^n by the discrete gradient $p_\sigma^n(u)$ to get the numerical flux in the form

$$\phi_\sigma^n(u_{h,k}^n) = (D_\sigma p_\sigma^n(u)) \cdot \mathbf{n}_{K,\sigma}. \tag{12}$$

$D_\sigma = D_\sigma^{n-1} = \begin{pmatrix} \bar{D}_{11}^\sigma & \bar{D}_{12}^\sigma & \bar{D}_{13}^\sigma \\ \bar{D}_{12}^\sigma & \bar{D}_{22}^\sigma & \bar{D}_{23}^\sigma \\ \bar{D}_{13}^\sigma & \bar{D}_{23}^\sigma & \bar{D}_{33}^\sigma \end{pmatrix}$ denotes an approximation of the mean value of the matrix D along σ which was evaluated at the previous time step using $u_{h,k}^{n-1}$. The elements of matrix D_σ are C^∞ functions due to the convolutions in (4) and (7).

Let us emphasize that in (12) we always consider the matrix D_σ written in the basis $(\mathbf{n}_{K,\sigma}, \mathbf{t1}_{K,\sigma}, \mathbf{t2}_{K,\sigma})$, cf. [2,3] for an analogy with the 2D model. In practice it means that, cf. Fig. 2, the matrix D given in the standard basis on a side σ by $\begin{pmatrix} D_{11}^\sigma & D_{12}^\sigma & D_{13}^\sigma \\ D_{12}^\sigma & D_{22}^\sigma & D_{23}^\sigma \\ D_{13}^\sigma & D_{23}^\sigma & D_{33}^\sigma \end{pmatrix}$ is the same in the new basis on two sides σ_W and σ_E. It has the form $\begin{pmatrix} D_{22}^\sigma & D_{12}^\sigma & D_{23}^\sigma \\ D_{12}^\sigma & D_{11}^\sigma & D_{13}^\sigma \\ D_{23}^\sigma & D_{13}^\sigma & D_{33}^\sigma \end{pmatrix}$ in the new basis for two other sides σ_S and σ_N and it becomes $\begin{pmatrix} D_{33}^\sigma & D_{23}^\sigma & D_{13}^\sigma \\ D_{23}^\sigma & D_{22}^\sigma & D_{12}^\sigma \\ D_{13}^\sigma & D_{12}^\sigma & D_{11}^\sigma \end{pmatrix}$ for the last two sides σ_B and σ_T. Using such matrix representations, the definition (12) can be written in the form

$$\phi_\sigma^n(u_{h,k}^n) = \left[\begin{pmatrix} \bar{D}_{11}^\sigma & \bar{D}_{12}^\sigma & \bar{D}_{13}^\sigma \\ \bar{D}_{12}^\sigma & \bar{D}_{22}^\sigma & \bar{D}_{23}^\sigma \\ \bar{D}_{13}^\sigma & \bar{D}_{23}^\sigma & \bar{D}_{33}^\sigma \end{pmatrix} \begin{pmatrix} \frac{u_E^n - u_W^n}{h} \\ \frac{u_{TN}^n + u_{BN}^n - u_{TS}^n - u_{BS}^n}{2h} \\ \frac{u_{TN}^n + u_{TS}^n - u_{BN}^n - u_{BS}^n}{2h} \end{pmatrix} \right] \cdot \begin{pmatrix} 1 \\ 0 \\ 0 \end{pmatrix} =$$

$$= \bar{D}_{11}^\sigma \tfrac{u_E^n - u_W^n}{h} + \bar{D}_{12}^\sigma \tfrac{u_{TN}^n + u_{BN}^n - u_{TS}^n - u_{BS}^n}{2h} + \bar{D}_{13}^\sigma \tfrac{u_{TN}^n + u_{TS}^n - u_{BN}^n - u_{BS}^n}{2h}.$$

Finally, let us summarize our **semi-implicit finite volume scheme**:

$$\frac{u_K^n - u_K^{n-1}}{k} - \frac{1}{m(K)} \sum_{\sigma \in \mathcal{E}_K \cap \mathcal{E}_{int}} \phi_\sigma^n(u_{h,k}^n) m(\sigma) = 0, \tag{13}$$

where

$$\phi_\sigma^n(u_{h,k}^n) = \bar{D}_{11}^\sigma \frac{u_E^n - u_W^n}{h} + \bar{D}_{12}^\sigma \frac{u_{TN}^n + u_{BN}^n - u_{TS}^n - u_{BS}^n}{2h} + \bar{D}_{13}^\sigma \frac{u_{TN}^n + u_{TS}^n - u_{BN}^n - u_{BS}^n}{2h}. \tag{14}$$

Due to the computation of the values u_{TN}, u_{TS}, u_{BN} and u_{BS} in (14) as the arithmetic mean of neighboring voxel values, we end up with the 27 point finite volume scheme.

4 Segmentation

Our segmentation approach is based on the subjective surface method [10] and its finite volume implementation from [9]. The mathematical model has the following form

$$\partial_t u = \sqrt{\varepsilon^2 + |\nabla u|^2} \nabla . \left(g(|\nabla G_\sigma * I^0|) \frac{\nabla u}{\sqrt{\varepsilon^2 + |\nabla u|^2}} \right), \quad \text{in } Q_T \equiv I \times \Omega, \tag{15}$$

$$u(x,0) = u_0(x), \quad \text{in } \Omega, \tag{16}$$

$$u = 0, \quad \text{on } I \times \partial\Omega, \tag{17}$$

where I^0 is the image which is segmented and ε is the regularization parameter. The solution u represents here the evolving segmentation function. The function $g = g(|\nabla G_\sigma * I^0|)$ has the role of the edge detector, which requires a suitable choice of g in practice, e.g. $g(s) = \frac{1}{1+Ks^2}$, $K > 0$.

In the subjective surface method we start the segmentation constructing the initial segmentation function located in an approximate object center. The segmentation function is driven by equation (15) and evolves to a numerical steady state. Its shock profile gives the segmentation result and shape of the object. To that goal, we choose a suitable isoline of the shock profile which represents the boundary of the segmented object. This isoline is most naturally taken as the average of maximal and minimal value of the final segmentation function.

5 Numerical Experiments

The goal of this section is to discuss our computational results and the influence of nonlinear tensor diffusion filtering on the time evolving biological structure segmentation. We perform our experiments on the 3D image sequences of cell nuclei, cf. Fig. 3, and cell membranes, cf. Figs. 4-6. The images represent early stages of the zebrafish embryogenesis and were created by the two-photon laser scanning microscope. We apply the 3D numerical scheme to filter the images,

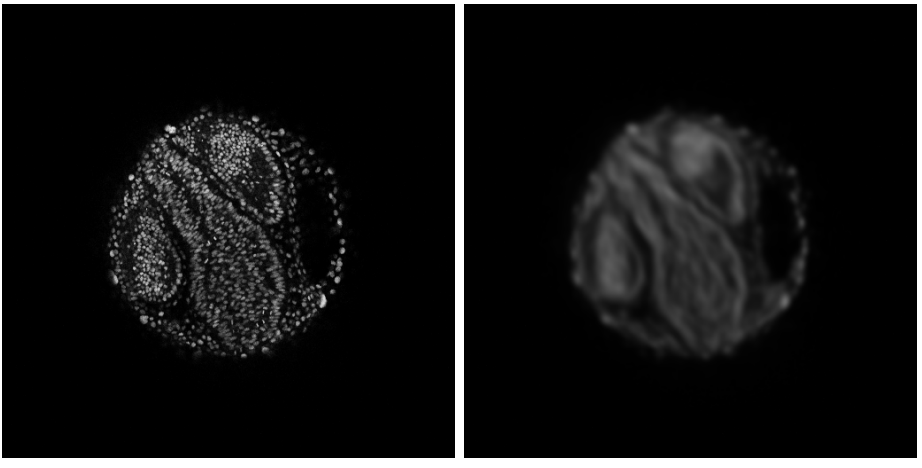

Fig. 3. 2D slices of a 3D zebrafish embryo image. Left: the original image. Right: the filtered image after 50 time steps.

then the segmentation is performed on 2D image slices (512×512 pixels) in order to firstly test the performance and capabilities of the method.

First experiment illustrates the behaviour of nonlinear tensor diffusion in filtering of this type of images, cf. Fig. 3. One can observe that this type of diffusion improves the connectivity of structure bordering lines while it smoothes the structure interiors. One can compare the original image showing separate nuclei but with observable structure borders with the filtered one, where the structure border lines are connected.

Our next experiments are devoted to the segmentation of eye retina structure in the several subsequent image slices. First, the initial segmentation function is given by two cones which are inside the structure such that their partially overlapping bases sufficiently cover the eye structure area. Then we evolved it in the original as well as filtered images. Using the original image we obtained the final state of segmentation function represented by a variety of different level lines, cf. Fig. 4 (top, right). The question is, which isoline would represent the most precisely the structure shape. The natural choice is a medium isoline which is depicted in the original image Fig. 4 (top, left). One can clearly see the large difference between the segmented and real structure shape due to the restraints of evolving segmentation function caused by inner cell structures. In order to compare our method with other filtering techniques we performed several tests. The segmentation results obtained on the images filtered by the geodesic mean curvature flow (GMCF) filtering, the mean curvature flow (MCF) filtering and the Perona-Malik (PM) filtering are shown in Fig. 5. In Fig. 5 (right), we can see that after filtering the profiles of final segmentation functions are not well suited for our purposes although the MCF results is rather close to the real one. They are again given by several different isolines and medium one, cf. Fig. 5 (left), represents the segmented structure only partially. This is a consequence of edge

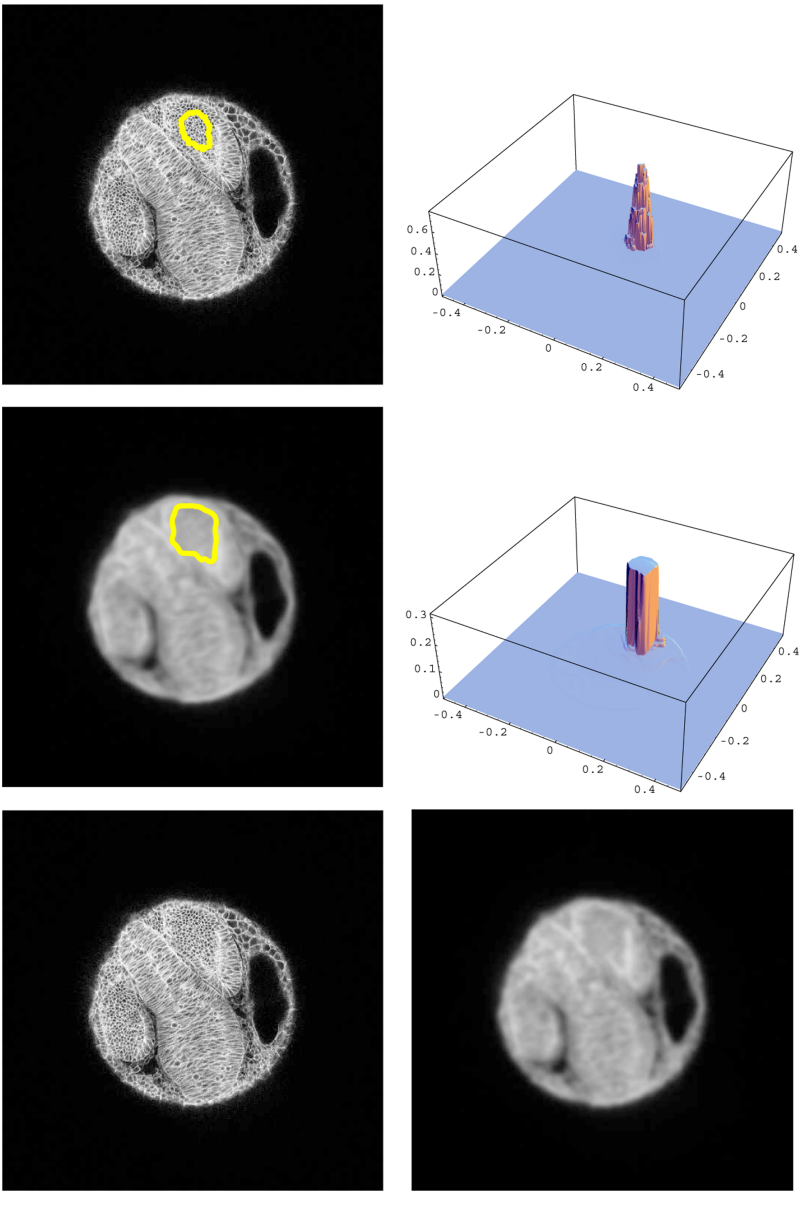

Fig. 4. The eye retina segmentation using the 2D original image (top) and image filtered by 20 time steps of the nonlinear tensor diffusion (middle). Left: the averaged isoline of the final state of segmentation function is superimposed to the original and filtered image, respectively. Right: the graphs of the final state of segmentation function is plotted after 2000 time steps using the original image and after 200 time steps using the filtered image. At the bottom we display the original (left) and the filtered image (right).

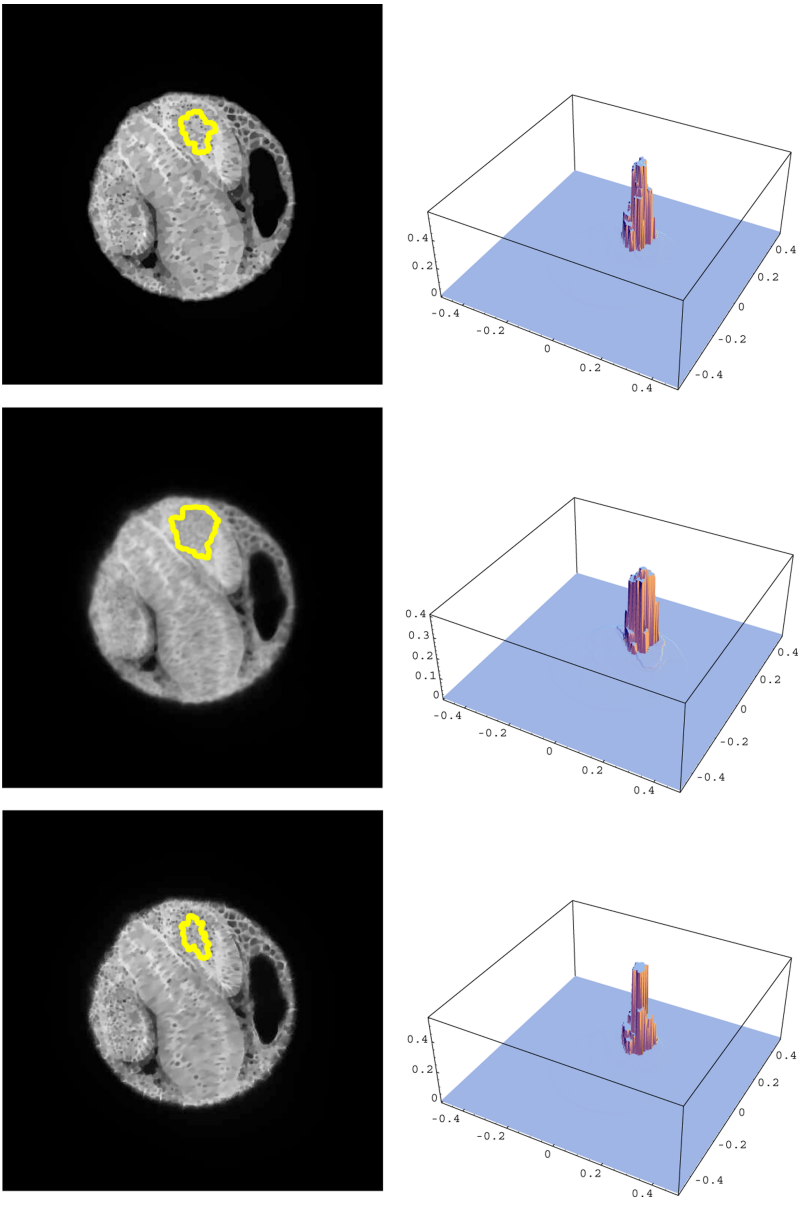

Fig. 5. The eye retina segmentation using the filtered image by 100 steps of the GMCF filtering (top), 25 steps of the MCF filtering (middle) and 20 steps of the PM filtering (bottom). Left: the averaged isoline of the final state of segmentation function is superimposed to the filtered image. Right: the graphs of the final state of segmentation function is plotted after 3000 segmentation steps using the GMCF filtering, after 500 segmentation steps using the MCF filtering and 5000 segmentation steps using the PM filtering.

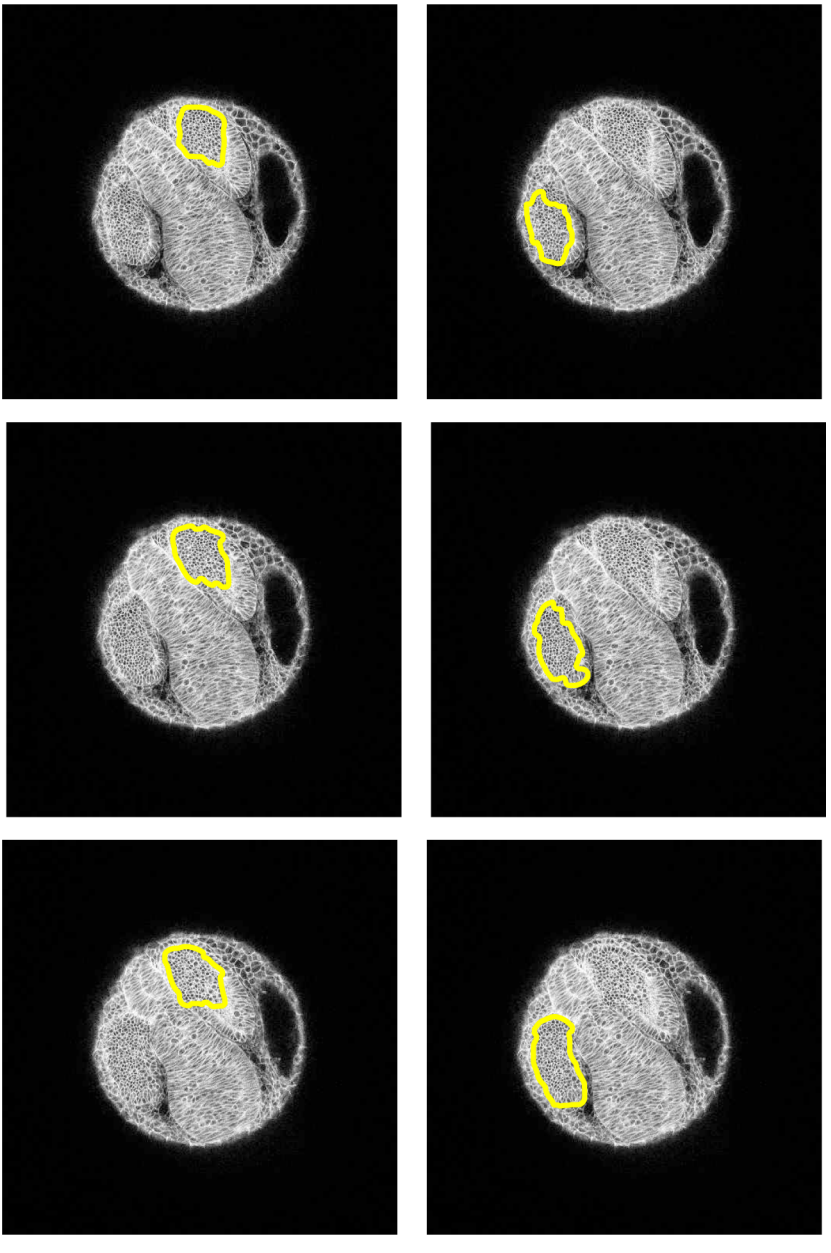

Fig. 6. The segmentation results for the image sequence which are superimposed to the original slices

preserving smoothing by GMCF and PM which can not remove inner cell structures. On the contrary, the final steady state of segmentation function evolving in the image filtered by nonlinear tensor diffusion consists of isolines accumulated

along the real structure boundary, cf. Fig. 4 (middle, right). The formation of correct shock profile was enabled due to the smoothing of cell structure barriers and noise removal and the emphasizing of structure boundaries. Embedding the medium isoline into the image, cf. Fig. 4 (middle, left) we achieved the precise structure shape.

Then the segmentation procedure was successively applied in the image sequence part consisting of 11 images, cf. Fig. 6. We use the backward in time strategy starting from the last image of the sequence segmented as explained above. The initial segmentation function for other slices is taken as the final result of the segmentation of the previous image. Fig. 6 shows the segmentation results displayed on the original membrane images from last 150th image slice (top), to the 145th slice (middle) up to the 140th slice of the processed image sequence (bottom).

In experiments dealing with the nonlinear tensor anisotropic diffusion we used the spatial step $h = 0.01$, time step $k = 0.0001$, $C = 1$, $\alpha = 0.001$, $\tilde{t} = 10^{-5}$, $\rho = 0.002$, 20 time steps for the filtering of membranes images and $\tilde{t} = 10^{-10}$, $\rho = 0.1$, 50 time steps for the filtering of nuclei images. The arising linear systems were solved by the Gauss-Seidel iterative method. For the segmentation experiments we use the following parameters: $\varepsilon = 10^{-4}$, the spatial step $h = 0.01$, time step $k = 0.01$, $\delta = 10^{-6}$ for a stopping criterion and $K = 100$ (a constant of the function $g(s) = \frac{1}{1+Ks^2}$), cf. [9]. The resulting linear systems were solved by the SOR method.

6 Conclusions

In the article we concern with the technique for embryo structure segmentation in image sequences. Since a noise and cell structures restrain the correct segmentation evolution, as the first step, we smooth the image sequence. We choose the nonlinear tensor diffusion due to the fact that this filtering not only smoothes image objects but emphasizes connections of their boundaries as well. Then, the segmentation process starts using an artificial initial function centered inside the biological structure of the first image in the sequence. The segmentation result given by the subjective surface method obtained for this image is used as the initial condition for the next image of processed sequence, etc. Our experiments confirm the usefulness of the nonlinear tensor diffusion for this type of segmentation.

Acknowledgment

The work was supported by the European projects Embryomics and BioEmergences, the grants APVV-RPEU-0004-06, APVV-0351-07, APVV-LPP-0020-07 and the grant of VEGA 1/0269/09.

References

1. Corsaro, S., Mikula, K., Sarti, A., Sgallari, F.: Semi-implicit co-volume method in 3D image segmentation. SIAM J. Sci. Comput. 28(6), 2248–2265 (2006)
2. Coudiere, Y., Vila, J.P., Villedieu, P.: Convergence rate of a finite volume scheme for a two-dimensional convection-diffusion problem. M2AN Math. Model. Numer. Anal. 33, 493–516 (1999)
3. Drblíková, O., Mikula, K.: Convergence Analysis of Finite Volume Scheme for Nonlinear Tensor Anisotropic Diffusion in Image Processing. SIAM J. Numer. Anal. 46(1), 37–60 (2007)
4. Drblíková, O., Mikula, K.: Semi-implicit Diamond-cell Finite Volume Scheme for 3D Nonlinear Tensor Diffusion in Coherence Enhancing Image Filtering. In: Eymard, R., Herard, J.M. (eds.) Finite Volumes for Complex Applications V: Problems and Perspectives, ISTE and WILEY, London, pp. 343–350 (2008)
5. Eymard, R., Gallouët, T., Herbin, R.: Finite Volume Methods. In: Ciarlet, P., Lions, J.L. (eds.) Handbook for Numerical Analysis, vol. 7. Elsevier, Amsterdam (2000)
6. Frolkovič, P., Mikula, K., Peyriéras, N., Sarti, A.: A counting number of cells and cell segmentation using advection-diffusion equations. Kybernetika 43(6), 817–829 (2007)
7. Meijering, E., Niessen, W., Weickert, J., Viergever, M.: Diffusion-Enhanced Visualization and Quantification of Vascular Anomalies in Three-Dimensional Rotational Angiography: Results of an In-Vitro Evaluation. Medical Image Analysis 6(3), 217–235 (2002)
8. Mikula, K., Peyriéras, N., Remešíková, M., Sarti, A.: 3D embryogenesis image segmentation by the generalized subjective surface method using the finite volume technique. In: Eymard, R., Herard, J.M. (eds.) Finite Volumes for Complex Applications V: Problems and Perspectives, ISTE and WILEY, London, pp. 585–592 (2008)
9. Mikula, K., Sarti, A., Sgallari, F.: Co-volume level set method in subjective surface based medical image segmentation. In: Suri, J., et al. (eds.) Handbook of Medical Image Analysis: Segmentation and Registration Models, pp. 583–626. Springer, New York (2005)
10. Sarti, A., Malladi, R., Sethian, J.A.: Subjective Surfaces: A Method for Completing Missing Boundaries. Proceedings of the National Academy of Sciences of the United States of America 12(97), 6258–6263 (2000)
11. Weickert, J.: Coherence-enhancing diffusion filtering. Int. J. Comput. Vision 31, 111–127 (1999)